Paper III

Three Dimensional Simulation of Robot path, Heat Transfer and Residual Stresses of a welded Part with Complex Geometry

M. Ericsson and P. Nylén and D. Berglund and R. Lin-Peng

Int. J. for the Joining of Materials 17(2) 2005

Three Dimensional Simulation of Robot path, Heat Transfer and Residual Stresses of a welded Part with Complex Geometry

M. Ericsson and P. Nylén and D. Berglund and R. Lin-Peng

Abstract

In this article a simulation system is presented that combines computer aided robotics software used to define the welding operation, with a finite element model that predicts temperature-time histories and residual stress distributions for welding applications. The objective is to develop a tool for engineering processes in which robot trajectories and welding process parameters can be optimized off-line on parts with complex geometries. The system was evaluated on a stainless steel gas turbine component. Temperature dependent properties and phase change were included in the analysis. The turbine component was welded using an in-house TIG welding cell. The assumptions and principles that underpin the modeling techniques are presented together with predicted temperature histories, residual stresses, and fixture forces. Predicted residual stresses were compared with neutron diffraction measurements.

Keywords: Off-line programming, Finite element analysis, Residual stress measurments

1 Introduction

A large number of aerospace components have complex shapes and are manufactured in several stages, often including joining operations performed by robots. Joining by welding, however, induces changes in the microstructures of the base metals and can generate unwanted stresses and deformation. To avoid deformations, expensive and complex fixtures often have to be used. Furthermore, the planning of optimal welding sequences in aerospace component welding is difficult and requires highly experienced operators. Programming of welding robots is usually performed manually by means of the 'jog teach' method. This method requires that the robot is off-line i.e. not used in production and that the part is stationary. The robot arm is jogged through the program under reduced power and at reduced speed, via a joystick. Generating a path by hand in this way can be time consuming. On a complex geometry, it is virtually impossible for a programmer to maintain a constant gun velocity and a constant distance from and orientation to, the part. Correct welding parameters i.e. parameters which generate a full penetration of the part, are usually derived by means of experimentation. Therefore a simulation tool that could be used for the evaluation of features such as structural behavior, welding sequences and

fixture solutions during the design stage would be desirable. The use of such a tool would make it possible to evaluate manufacturing processes in the early stages of product development and would reduce both the number of welding experiments required and the need for welding operator experience. The tool should preferably be capable of simulating a number of facets of the process including the welding torch path, the detection of collisions between the torch and workpiece, and the optimization of welding parameters and fixture solutions relating to penetration and component deformation behavior. Thus, a combination of the simulation techniques, finite element analysis (FEA) and computer aided robotics (CAR) is necessary.

FEA simulation of thermal history, residual stresses and distortion has been performed since the early 1970s and several papers have been presented [1-6]. Large complex simulation models of three-dimensional components are however still rare, mainly due to the lack of computational power. The underlying reason is that, in order to be able to compute temperature and residual stress fields in the affected zone, a very fine discretization of the space variable is required to properly accommodate sharp gradients.

The CAR technology is also well known and has been an established research area for many years [7, 8, 9]. Using this technique, the programming of the robot is transferred from the workshop to a computer system where the programming can be performed without disturbing production. The technique can be used to simulate the welding torch path, to detect torch-workpiece and torch-fixture collisions, and to control torch orientation as well as electrode distance.

In this project an integrated approach, using two commercial CAR and FEA codes, making it thus possible to optimize torch trajectories, weld parameters and fixture solutions off-line, is described. The best welding parameters, i.e., the parameters that generate the lowest component deformation while keeping full penetration, can thus be found. The objective of this project is to describe the principles upon which the system is based and to demonstrate some of its capabilities. The principle of the OLP-FEA integration which previously has been presented in [10] is summarized here for the sake of completeness.

2 Integration of CAR and FEA

The overall principle of the integrated system is given in Figure 1. The following steps describe the procedure:

1. The component to be manufactured is created in a CAD/CAM system.
2. The model in step one is imported to the OLP software and the FEA software, either using a direct translator or by using a neutral file format, such as IGES or STEP. In the CAR software a model of the work cell is created. A welding program (including robot motion, weld speed, and arc current, etc.) is developed. Checks for collisions are also conducted.
3. The welding parameters, i.e., robot poses, weld speed and arc current, are exported from the CAR software to the FEA software using an interface developed as part of

this project.

4. Thermal histories and residual stresses are predicted in the FEA software. An optimization of weld velocity is performed to generate the lowest component deformation while keeping full penetration.

5. The optimized welding parameters are exported to the robot motion program. A translation of the program to a specific robot manufacturer language is carried out.

6. The final program is downloaded to the manufacturing equipment (robot and weld controller systems).

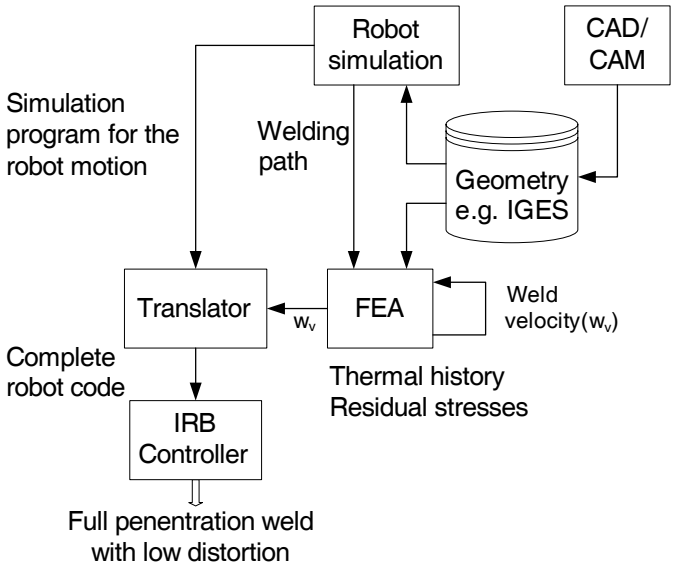

Figure 1: *Simulation system architecture.*

A more detailed description of the principles of the robot simulation (CAR), step two above, and the FEA simulation, step four, is provided in the following sections.

3 Computer Aided Robotics

Several commercial software packages for CAR exist (GRASP, IGRIP and Robcad etc.). The procedure using these systems can be summarized by means of the following steps. A more detailed description can be found in [7].

1. Modeling of the work cell

2. Work cell calibration

3. Programming of robot, positioner and other optional work cell equipment
4. Downloading of the program to the robot controller
5. Additional robot programming
6. Test running

The first step involves the construction of a geometrical model of the workpiece, including both a geometrical and a kinematic model of the work cell. These models are constructed using drawings, CAD/CAM models, or if such not are available, by obtaining measurements of all the critical equipment positions in the cell. If this model is created in a CAD system the data is imported to the CAR software either using a neutral interface (for instance IGES) or a direct reader. The work cell model might, alternatively, be constructed directly in the CAR system. Normally, kinematic models as well as geometric models of robots are pre-defined by the software manufactures.

In the second step a calibration of the model with the real cell is performed. This step can include several sub steps, such as tool point, work piece and signature calibration. [7]. Tool calibration is performed in order to determine the tool center point and to determine the weld torch orientation. A procedure using a measuring arrow in a fixed position in the work cell and moving the robot to this position in different directions is usually used. The positions from the real robot cell are then uploaded to the CAR software and a “best fit” is found using regression. The calibration of the workpiece and other critical components such as fixtures is performed similarly by moving the robot to identified positions on the component. These positions are recorded and uploaded to the OLP software where a similar adjustment of the model is made. To find errors in the geometrical model of the robot, an arm signature calibration can be used. This calibration finds any deviation in the length of the robot joints and in the zero points for the joints. A more accurate calibration of the work cell can be obtained using an advanced external measuring system, such as a laser measuring system.

In step three the robot motion is programmed using either a high level language or a specific robot language. If a high level language is used, the program is translated to the specific robot language and downloaded (step four) to the robot controller system.

Usually equipment specific additional programming is needed (step five), which is performed manually at the robot. Validation of the program by test runs is finally performed in step six.

The IGRIP (Interactive Graphics Robot Instruction Program, Deneb Robotics) system was used in this study. A tool calibration and a workpiece calibration were performed using the robot arm. Calibration of other objects, such as the welding table were performed using measuring tape. The high level language GSL, which is the graphical simulation language in IGRIP, was used for programming all of the devices in the cell. The programmed part was a section of an aerospace part, a turbine component from the V2500 engine provided by the Volvo Aero Cooperation. A 1/13 sized piece was cut out of the original part, which originally consisted of an inner and an outer ring and 13 vanes, see Figure 2a. Both the outer and inner ring were welded onto a steel plate, which acted as a fixture. The vane was

tack-welded between the outer and inner ring using manual TIG welding. The welding paths, including initial weld velocities, were then exported to the finite element software where predictions of temperature histories, residual stresses and fixture reaction forces were performed. The principle of this model is described in the next section.

Figure 2: *a) Turbine component consisting of an inner- and an outer ring and 13 vanes. b) experimental component (1/13 of the turbine component).*

4 Finite Element Analysis

Numerical methods have been used since the beginning of 1970's to simulate the welding process [1-6]. The main focus has been to predict thermal histories, residual stresses and distortion. Different assumptions and simplifications have to be considered when building an FEA model. Examples of areas that have to be considered are part geometry simplifications, the type of material to be used in the model, load conditions, heat transfer and other boundary conditions and, in addition, numerical strategy. In this project the commercial FEA program MARC from MSC Software was used. The model contained 3056 shell elements and 3182 nodes, see Figure 3. A staggered approach was used for the coupled thermal-mechanical simulation. This means that the updating of the geometry used in the thermal calculation is lagging one time step behind.

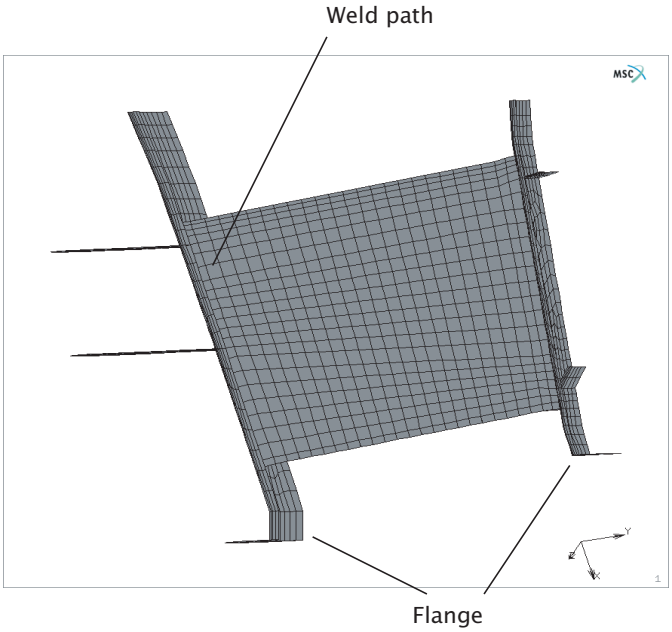

Figure 3: *Shell model of experimental component.*

4.1 Boundary Conditions

All FEA problems are defined in terms of initial and boundary conditions. A typical type of initial condition for a welding application is the initial temperature that, in most cases, is set to room temperature. Examples of the most important boundary conditions are fixture forces and heat transfer coefficients between the part and its surroundings. A model of the arc between the electrode and the part is usually too complex to be integrated in the same model. The most common method is to use a moving heat source. User

subroutines were therefore developed to simulate a moving Gaussian surface distribution [4]. This distribution was preferred over a volumetric one since it reduces the number of parameters to be fit and because the plates to be welded were considered thin (<1.5mm). The heat flux was expressed as [4]:

$$q = \frac{\eta E I \alpha_q}{\pi} \mathrm{e}^{-\alpha_q r^2} \tag{1}$$

where q denotes the heat transferred to the workpiece, E the voltage, I the current, η the efficiency factor, q the concentration factor, and r the radial distance from the center of the heat source. The distribution was truncated in the radial direction, at a cut off limit of 5% of the maximal heat input, as proposed by D. Radaj [4].

Natural convection was only used as the heat transfer boundary condition between the part and the surrounding environment. The flanges on the *Inner*- and *Outer ring*, see Figure 2a, were assumed to be clamped in the model since no fixture was used. The *Inner*- and *Outer ring* were instead welded on a steel plate, see Figure 2b.

4.2 Material properties

The initial microstructure of the material consists of a mixture of ferrite and pearlite. In the numerical model the ferrite/pearlite to austenite transformation was assumed to occur only if the highest temperature experienced by the material was greater then the A_{e3} temperature, Figure 4. Since the cooling rate of any austenite phase formed during welding is always higher than 0.3 °C/s between the A_{e3} and martensite start temperature, it can safely be assumed that all austenite is transformed to martensite irrespective of cooling rate. This assumption is supported by the results of the thermal dilatation for specimens heated at 100 °C/s and then cooled at 10 °C/s, and at 0.3 °C/s, see Figure 4.

Both cases gave the same amount of martensitic transformation. It should be noticed that it is assumed that pure martensite is formed. It should also be noticed that the martensite start temperature, Point 1 in Figure 4, decreases when the cooling rate is increased. This has not been accounted for in the numerical model. The thermal dilatation for reheated martensite follows the martensite curve, Figure 4.

A thermo-elastoplastic model based on von Mise's theory was used. It was assumed that no creep strains occur during welding since the material is exposed to a high temperature for a very short period of time. The hardening behaviour of the material was assumed to be isotropic and linearly piecewise. Transformation plasticity was not accounted for in the model. The temperature dependent Young's modulus and Poisson's ratio are shown in Figure 5. Figure 5 also shows the virgin yield limit for the initial ferrite/pearlite mixture, σ_{yf}, and the yield limit of pure martensite, σ_{ym}.

The yield limit of the material changes due to the phase transformation from ferrite/pearlite to martensite. If the peak temperature during welding had been higher than 850 °C (A_{e3}) the yield limit would have followed the curve for martensite when the material is cooled. The curve denoted σ_{yf} in Figure 5 is followed during cooling if the peak temperature had

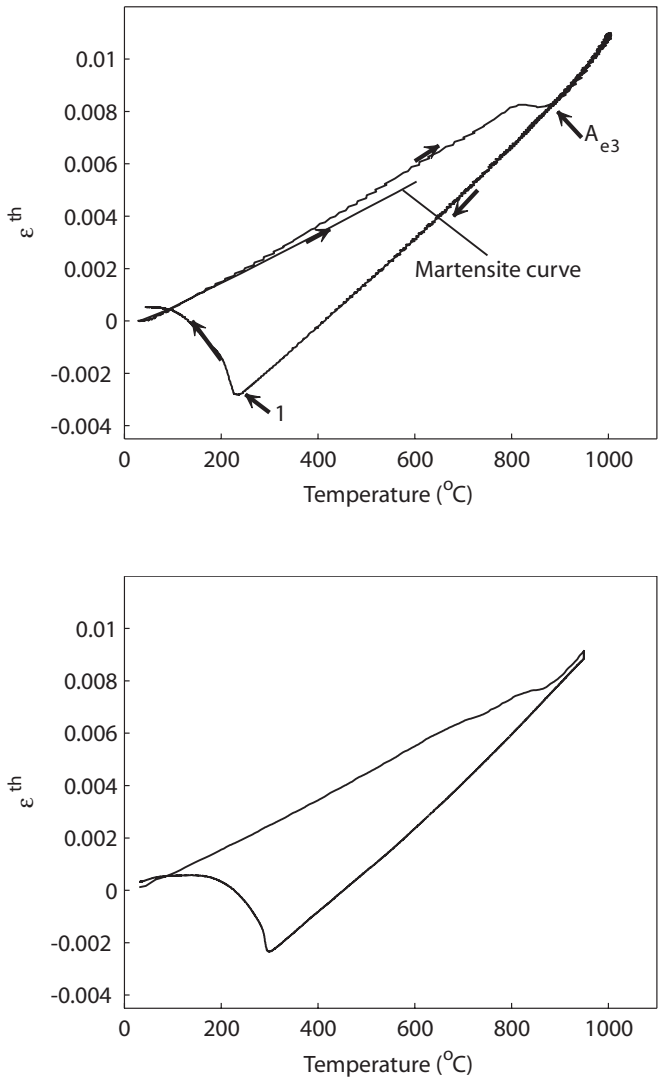

Figure 4: *Thermal dilataion, ε^{th} vs. temperature for, (above) a cooling rate of 10 °C/s, (below) a cooling rate of 0.3 °C/s.*

been lower than the A_{e3}-temperature. To avoid convergence problems in the numerical calculations, the minimum yield limit was set to 20 MPa and the maximum Poisson's ratio to 0.45. The temperature-dependent thermal properties are shown in Figure 6. The thermal conductivity was increased by a factor of 4.7 when the temperature reached the liquidus temperature to account for connective heat transfer in the melted zone [4]. This

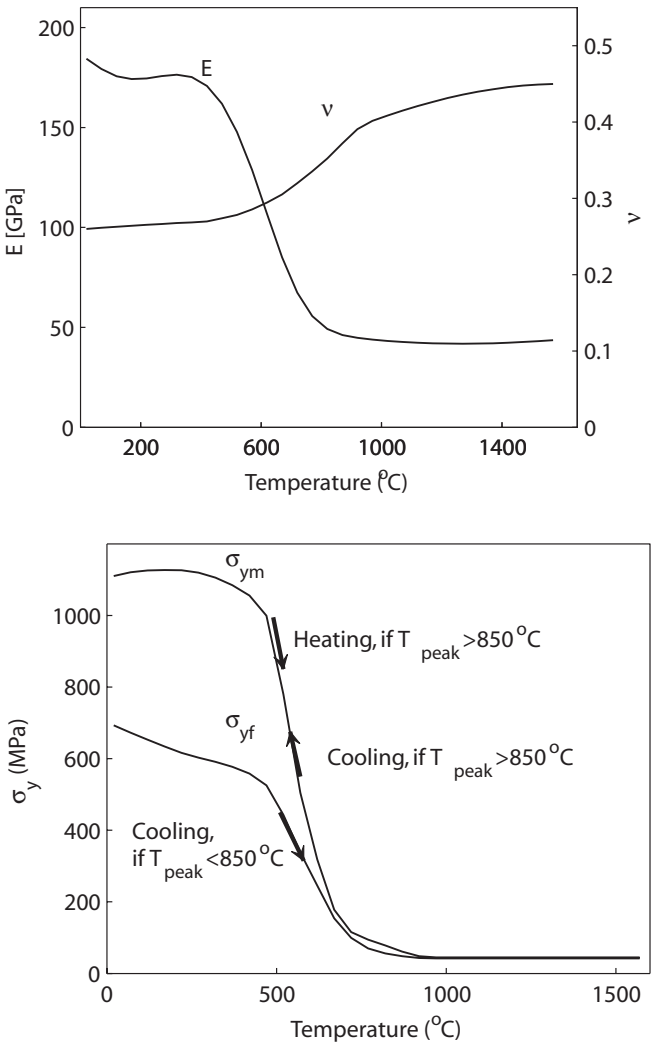

Figure 5: *Temperature dependent mechanical properties, (above) Young's modulus, E, and Poisson's ratio, ν, (below) Temperature dependent yield limit for the ferrite/pearlite phase, σ_{yf}, and yield limit for the martensitic phase, σ_{ym}.*

simplified model was used instead of more advanced CFD models to simulate the physics in the molten zone, since the latter methods are computationally too demanding. The latent heat of melting was set to 338 kJ/kg, $T_{solidus}$ to 1480 °C and $T_{liquidus}$ to 1600 °C. The emissivity factor used for the radiation boundary condition is shown in Figure 6.

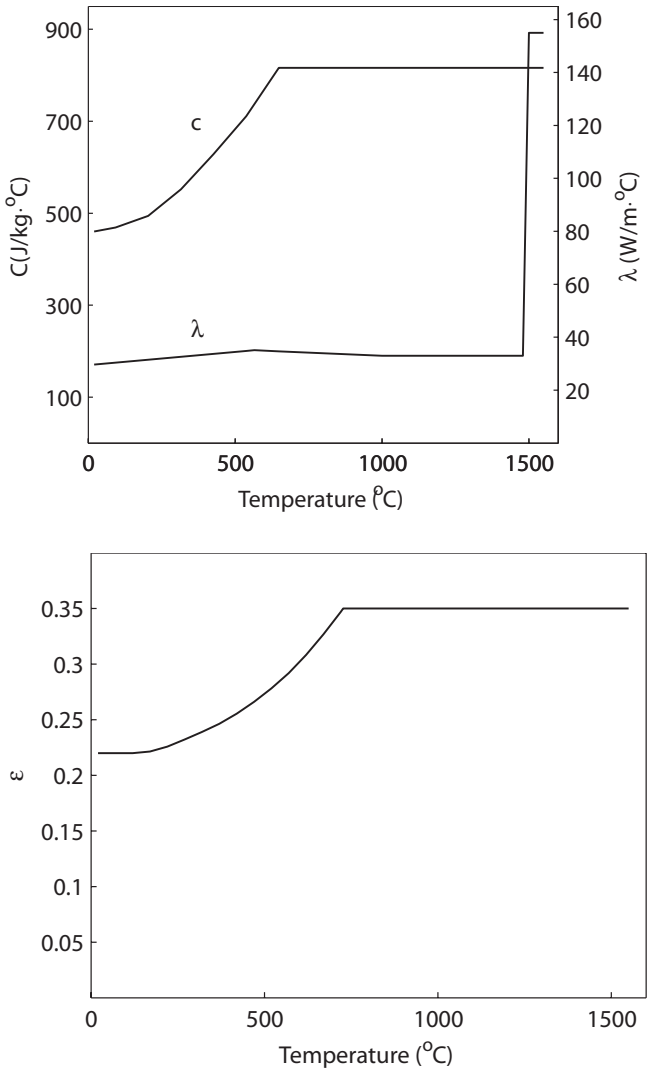

Figure 6: *(left) Temperature dependent conductivity λ, and heat capacity C. (right) Emissivity.*

5 Experimental

The component was TIG welded using an in-house robotised welding cell. The torch used is from Binzel AB (thoriated tungsten electrodes) and lined to a six-axis robot, ABB IRB 1400. The power source is a TIG Commander 400 AC/DC from Migatronic AB. The vane was spot-welded between the outer and inner ring prior to the welding of the seam.

Argon gas was used, both on the topside and on the root side to avoid oxidation of the component. No filler material was used during the welding. A welding speed of 2.5 mm/s and a welding current of 80 A were used during the experimental.

The residual stresses measurements were performed on the dedicated neutron diffractometer REST [11] at the Studsvik Neutron Research Laboratory, Sweden. The principle of strain measurement by neutron diffraction is shown in Figure 7. In a typical neutron diffraction experiment a collimated neutron beam, of wavelength λ, is diffracted by the polycrystalline sample and passed through a second collimator to the detector. The slits of the two collimators define the gauge volume.

Knowing the wavelength λ of the monochromatic neutron beam and measuring the 2θ angle corresponding to the maximum value of the intensity in the obtained diffraction peak, the interplanar distance d_{hkl} (where h, k and l are the Miller indices of the investigated lattice plane) can be evaluated using Bragg's law:

$$\lambda = 2d_{hkl}\sin\theta \tag{2}$$

The corresponding lattice strain is defined as:

$$\varepsilon_{hkl} = \frac{d_{hkl} - d_0}{d_0} \tag{3}$$

where d_0 is the interplanar distance in a stress-free material. For an isotropic material, the residual stresses are calculated using Hooke's law which, in case of triaxial (x, y, z) measurement is written as:

$$\sigma_i = \frac{E}{(1+\nu)(1-2\nu)}[(1-\nu)\varepsilon_i + \nu(\varepsilon_j + \varepsilon_k)] \tag{4}$$

with i, j, k corresponding to x, y, z and where E is Young's modulus and ν is Poisson's ratio. If the stress along the specimen normal, σ_{33}, can be assumed to be zero, a so-called $\sin^2\psi$ technique [12] can be employed for residual stress analysis. For such a bi-axial stress state, the in-plane stress parallel to ϕ (Figure 7), σ_ϕ, is correlated to the measured strain along a sample direction (ϕ, ψ) by the following equation [12].

$$\frac{d_{\phi\psi} - d_0}{d_0} = \left(\frac{1+\nu}{E}\right)\sigma_\phi \sin^2\psi - \frac{\nu}{E}(\sigma_{11} + \sigma_{22}) \tag{5}$$

where σ_{11} and σ_{22} are the stress components parallel to the in-plane specimen co-ordinates. For the definition of (ϕ, ψ), see Figure 7. The stress can be calculated from the slope of $d_{\phi\psi}$ vs. $\sin^2\psi$ distribution. The d_0 can be replaced by the measured interplanar spacing along $\psi = 0^\circ$ without introducing significant error. More details on stress analysis by means of diffraction measurement can be found in [12].

The Fe-(211) plane was used for the transverse stress measurement. With a nominal wavelength of 1.7 Å, the diffraction angle was found to be about $2\theta = 93.5^\circ$. The slit

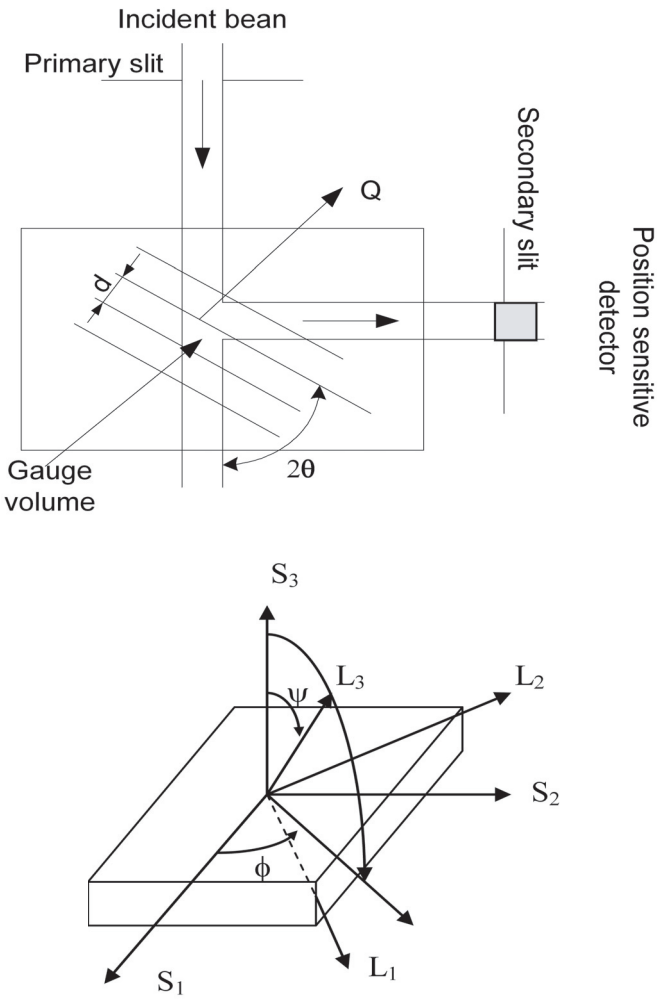

Figure 7: *A schematic representation of the strain measurement by neutron diffraction and the specimen co-ordinate system used for stress analysis with L3 indicating the direction of measured strain.*

size was 0.5 mm (width) by 10 mm (height) with the length of the gauge volume parallel to the weld. The diffraction peak of martensite is inherently broad and, to avoid a peak clipping effect due to the use of a small slit width, the position sensitive detector was scanned at 15 positions to map a diffraction peak. The peak centre was determined by fitting a Gaussian function to the measured diffraction data. As the residual stress state can reasonably be assumed to be bi-axial, the in-plane residual stress was calculated using Equation (6) with a diffraction elastic constant, $\frac{1+\nu}{E} = 5.81 \cdot 10^{-6}$ MPa^{-1} [13]. Due to the complex component geometry, measurements could only be made at $\psi = 0^\circ$ and 90°,

respectively. The uncertainty of sample positioning was estimated to be ± 0.2 mm for the transverse direction and less than to ± 0.1 mm for the normal direction.

6 Results and Discussion

The results of the robot program conducted off-line revealed a high degree of accuracy and very few adjustments after the calibration were required. A validation study of temperature predictions for the specific part using thermocouples and infrared camera measurements had been performed on a prior occasion. A typical example of predicted temperature-time histories, located at 4.2, 6.3 and 8.4 mm respectively from the weld centerline, is given in Figure 8.

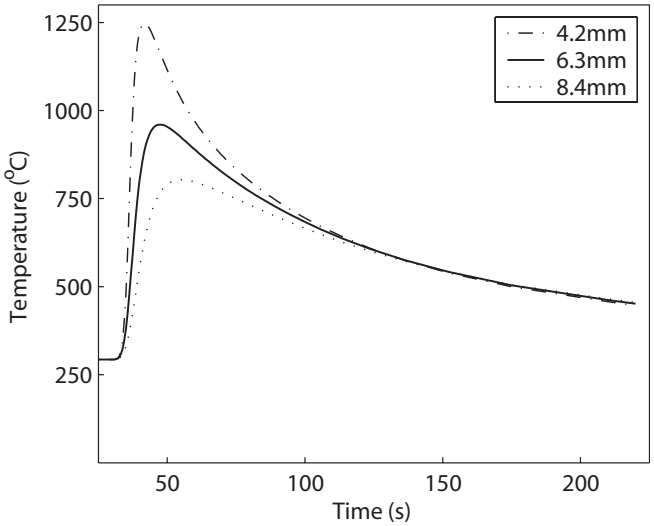

Figure 8: *Temperature histories in three points along a perpendicular line to the weld seam.*

Residual stresses were evaluated along three lines, located at the front, in the middle and at the back of the weld, Figure 9. The predictions are summarized in Figures 10 and 11 along each line. Figure 10 shows the calculated longitudinal stresses (i.e. in the weld direction) and Figure 11 the stresses perpendicular to the weld direction. Since a shell model was used, the stresses in the thickness direction are zero. The length axis in Figures 10 and 11, represents the distance from the weld center and the stresses shown were recorded after 200 s from the start time of the welding. The longitudinal stress level and distribution are similar along all sampling lines and the maximum longitudinal stress is about 800 MPa. The stress components perpendicular to the weld direction at different reference line locations show large differences. Compressive stress is generated both along the middle- and back reference line but this is not the case for the front line.

The reason for these differences is due to the difference in stiffness of the component along the seam.

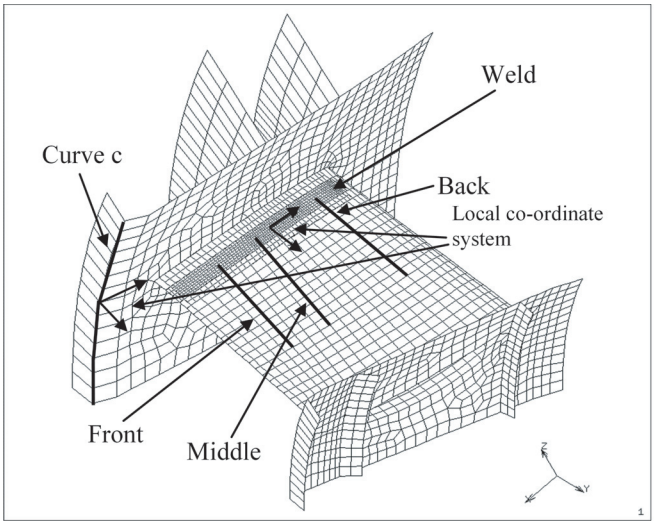

Figure 9: *Lines where evaluations were performed.*

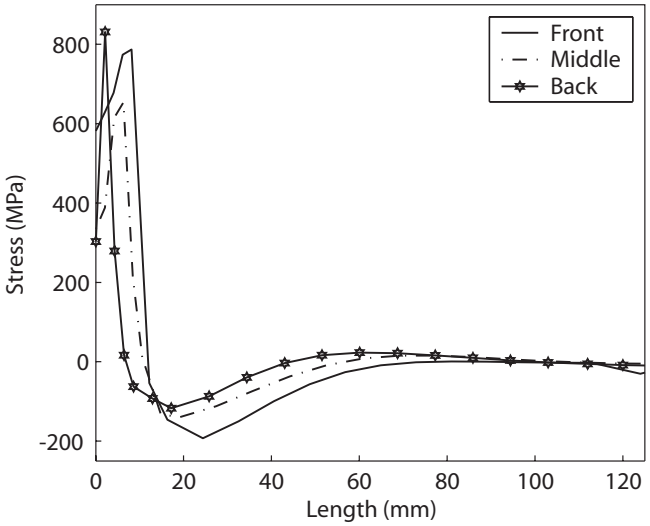

Figure 10: *Predicted longitudinal stress component along the three lines in Figure 9.*

Figure 12 show the diffraction peak with as Full Width at Half Maximal intensity (FWHM), measured in both normal direction, as a function of increasing distance from the weld center line. The distribution of the peak width indicates that microstructure in the weld and

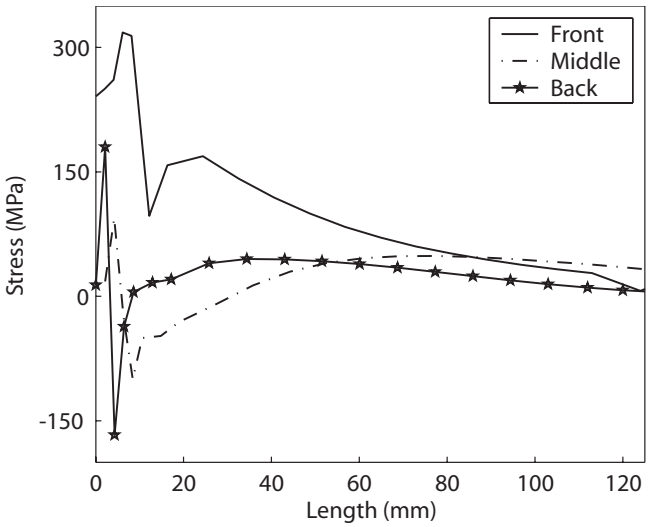

Figure 11: *Predicted stress component (perpendicular to the weld) along the three lines in Figure 9.*

the heat affected zone (HAZ) is essential martensite and its volume decreases rapidly at about 5 mm from the weld. This agrees well with the simulation result. The derived residual stresses are plotted in Figure 13.

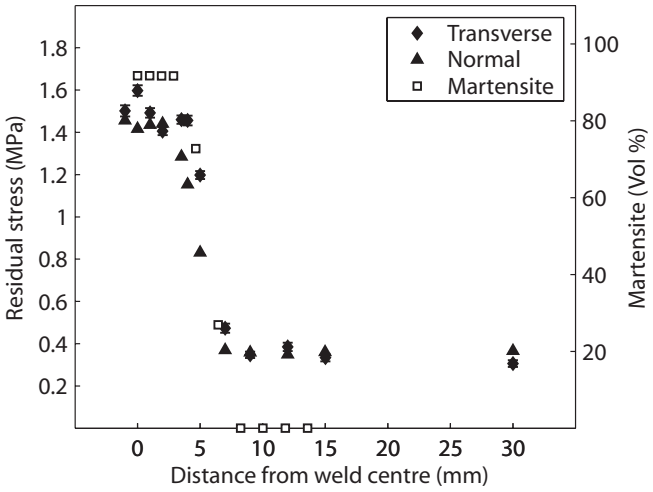

Figure 12: *Comparison of the measured distribution of diffraction peak width (FWHM) and simulated volume of martensite.*

The residual transverse stress distribution derived from the measured diffraction peak

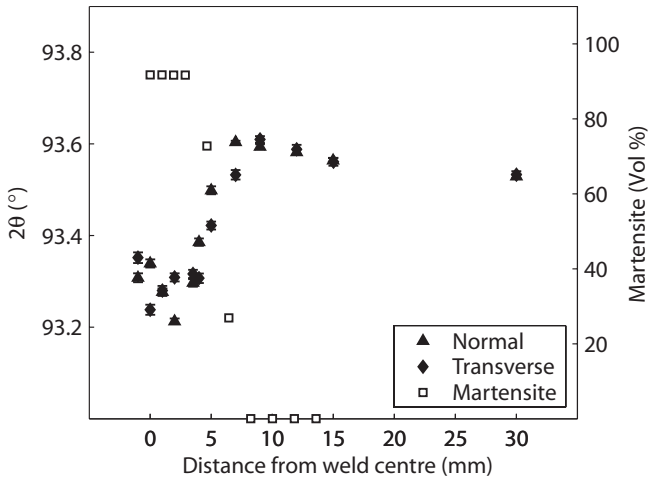

Figure 13: *Variation of diffraction peak centre line with increasing the distance from weld centre for the normal and transverse direction, respectively.*

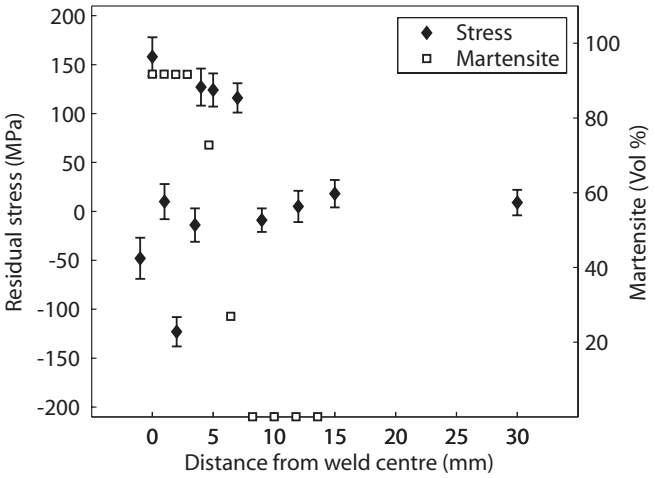

Figure 14: *Measured transverse stress distribution.*

centre (Figure 13) is plotted in Figure 14. Figure 15 compares the predicted and measured residual stresses are compared in Figure 14. The discrepancy between the measured and predicted results shown in Figure 14 has a number of possible explanations that relate to the finite element model:

- A simplified model for the phase transformation has been used
- The model did not include a transformation induced due to plasticity

- The model did not include plasticity

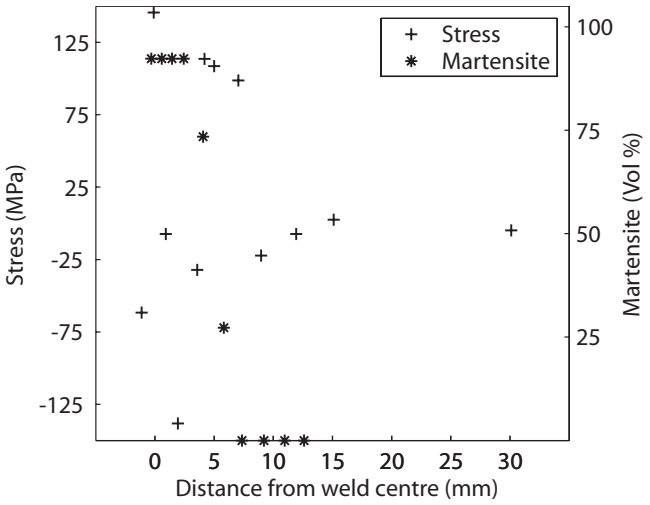

Figure 15: *Comparison between simulation and measurement residual stresses.*

One other reason for the discrepancy can be due to the repositioning of the component between the transverse and the normal measurement. This may lead to errors, particularly in the heat affected zone, where the peak centre, and thus the lattice parameter, change rapidly. However this error can not explain the observed oscillation. Due to the large scatter in the transverse stress measurements in the heat affected zone, no specific conclusion can be arrived at. There is a fairly good agreement outside this zone.

Reaction forces in a rectangular coordinate system located in a point along the weld between the outer ring and steel plate, see Figure 2b, are shown in Figure 16. The forces are an example of a result that can be used to evaluate fixture solutions on a real part. Another example of an application of the model given in Figure 17, where an optimization of the weld velocity to generate the lowest component deformation while keeping full penetration, was conducted.

Several developments of the FEA models are possible. One simplification in the present model is that the tack welding (performed before the main weld) was not considered. This tack welding will most probably affect the stress level. The development of a new solid model, instead of a shell model, including these tack welds is planned. Including transformation plasticity in the material model will also lead to a change in the stress state [6].

The present model can, however, function as a powerful tool to qualitatively evaluate different weld parameters and fixture designs off-line.

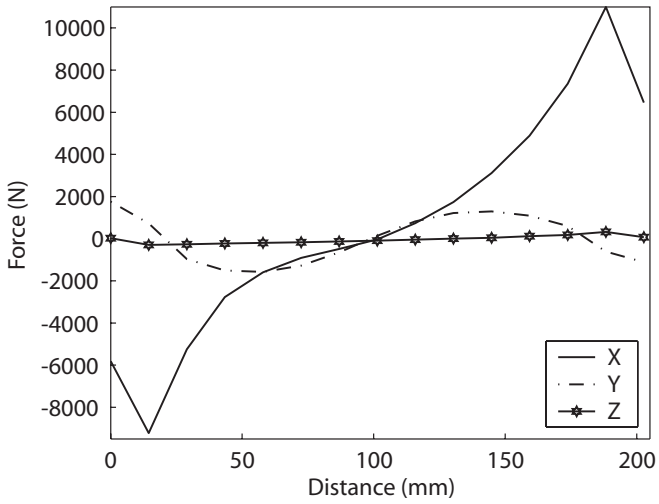

Figure 16: *Reaction forces along curve c, Figure 9, between the outer ring and the steel plate.*

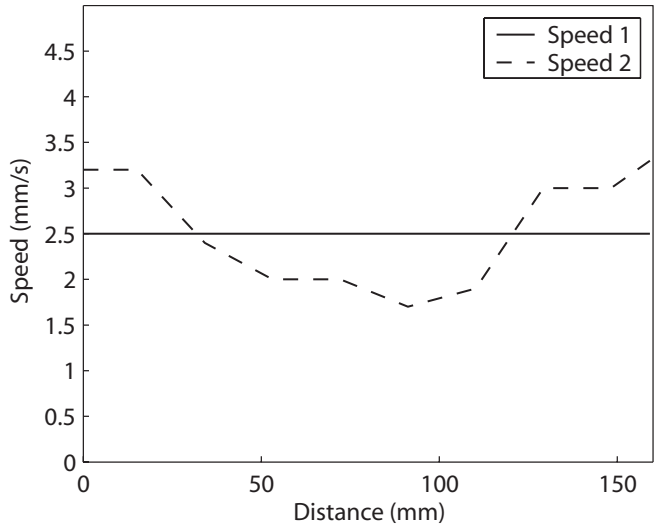

Figure 17: *Weld velocity before (solid) and after (dashed) optimization.*

7 Summary and Conclusions

A simulation tool to define robot trajectories and to predict thermal histories and residual stress distributions on parts with complex geometries has been developed. The tool

was evaluated on a part with a complex shape where robot weld paths were defined off-line, automatically downloaded to an FEA-model, where transient temperatures, residual stresses and fixture reaction forces were predicted. Residual stresses on the component were measured using neutron diffraction and compared with predicted residual stresses and fairly good agreement was found. The method described seems to provide a powerful tool for the construction and optimization of torch trajectories and process parameters off-line.

Acknowledgements

The authors wish to acknowledge the assistance in the development of the material models by Andreas Lundbäck of LuleåUniversity of Technology. Mr. Alastair Henry of University of Trollhättan/Uddevalla for linguistic revision. Mr Xavier Guterbaum of University of Trollhättan/Uddevalla for all our valuable discussions in the robot laboratory. The work was funded by the Foundation for Knowledge and Competence Development and EC Structural Funds.

8 References

1. Y. Ueda and T. Yamakawa, Analysis of thermal elastic-plastic stress and stress during welding by finite element method, Trans. JWRI, Vol. 2 (90-100, (1971).
2. Y. Ueda and T. Yamakawa, Thermal stress analysis of metals with temperature dependent mechanical properties, Proc. of Int. Conf. on Mechanical Behavior of Materials, Vol. III,10-20, (1971).
3. H.D. Hibbit and P.V Marcal., A numerical thermo-mechanical model for the welding and subsequent loading of a fabricated structure, Comp. & Struct., Vol. 3 1145-1174 (1973).
4. Radej, D. Heat Effects of Welding, p33, Springer Verlag, Berlin (1992)
5. T.W Eagar, N.S. Tsai, American Welding Society Journal 62(12) 346-s to 355-s. (1983)
6. F.G. Rammerstorfer, D.F Fischer, W. Mitter, K.J Bathe and M. D. Snyder, On thermo-elasto-plastic analysis of heat-treatment processes including creep and phase changes, Comput. Struct., Vol 13, 771-779. (1981).
7. G. Bolmsjö, M. Olsson, K. Brink, Off-line programming of GMAW robotic systems - a case study. Int. J. for the Joining of Materials, Vol. 9 (3), 86-93, (1997).
8. S Walter Simulation and Calibration for Off-line Programming of Industrial Robots, paper 54, Proc. of Computer Technology in Welding, Paris, June 1997.
9. R.O. Buchal, D.B. Cheras, F. Sassani, J.P. Duncan, Int. J. of Robotics Research 8 (3): 31-43 (1989).

10. M. Ericsson, P. Nylén, G. Bolmsjö, Three-Dimensional Simulation of Robot Path and Heat Transfer of a TIG-welded Part with Complex Geometry, 11th International Conference on Computer Technology in Welding, Colombus, Ohio, Dec. 2001.

11. R. Lin and K. Sköld, The Neutron Diffraction Facility for Residual Stress Measurements in Studsvik, in Proc. of the 4th European Conf. on Residual Stresses, Cluny en Bourgogne, France, pp. 145-152, 1996.

12. I. C. Noyan, J. B. Cohen, Residual Stress. Measurement by Diffraction and Interpretation. Springer-Verlag, 1987.

13. B. Eigenmann und E. Macherauch: Röntgenographische Untersuchung von Spannungszuständen in Werkstoffen, Mat.-wiss.u. Werkstoffech. 27, 426-437 1996.